Nano Research

Open Access

Research Article

Poly(β-ketoenamine) membranes with interconnected microporosity for high-performance fluid separations

Binyu Zhou[1], Guishan Hu[1], Yubo Cui[1], Miaomiao Tian[2] ✉, Xueli Cao[3,4], Shi-Peng Sun[3,4], Jingwei Hou[5], Yatao Zhang[1], Bart Van der Bruggen[6], and Junyong Zhu[1] ✉

[1] *School of Chemical Engineering, Zhengzhou University, Zhengzhou 450001, China*
[2] *School of Ecology and Environment, Zhengzhou University, Zhengzhou 450001, China*
[3] *State Key Laboratory of Materials-Oriented Chemical Engineering, National Engineering Research Center for Special Separation Membranes, Jiangsu National Synergetic Innovation Center for Advanced Materials, College of Chemical Engineering, Nanjing Tech University, Nanjing 211816, China*
[4] *NJTECH University Suzhou Future Membrane Technology Innovation Center, Suzhou 215100, China*
[5] *School of Chemical Engineering, The University of Queensland, St Lucia, QLD 4072, Australia*
[6] *Department of Chemical Engineering, KU Leuven, Celestijnenlaan 200F, B-3001 Leuven, Belgium*

Cite this article: *Nano Research*, **2026**, *19*, 94908385. https://doi.org/10.26599/NR.2026.94908385

ABSTRACT: Thin-film composite (TFC) membranes fabricated via interfacial polymerization are a pivotal enabler for energy-efficient fluid separations. However, achieving both a high separation efficiency and solvent stability is challenging, as it requires the critical and precise tuning of the film microporosity and internal molecular interactions. Here, we present a molecular linkage engineering approach to designing high-microporosity and structurally rigid poly(β-ketoenamine) membranes. By integrating a three-dimensional (3D) shape-persistent triptycene scaffold (2,6,14-triaminotriptycene, TAT) and a hydroxyl-pendant trialdehyde linker (1,3,5-triformylphloroglucinol, Tp), the resultant TAT-Tp membranes exhibit an extraordinary surface area of 620.21 $m^2 \cdot g^{-1}$, far exceeding those of traditional polyamide and polyimine counterparts. The high density of β-ketoenamine linkages promotes the creation of intra- and intermolecular hydrogen-bonding networks, thereby imparting remarkable structural stability and inducing ordered local regions. These improved structural attributes, coupled with high microporosity, endow these membranes with dual-function superiority: 99.1% desalination efficiency and 99.2% methyl orange rejection in methanol. Furthermore, the membranes exhibit a remarkable solvent resistance, retaining structural integrity after 30-d exposure to diverse solvents. Experiments and simulations reveal the critical role of substantially interconnected ultramicroporous voids within the rigid crosslinked networks in achieving this superior performance. This work provides a framework for engineering resilient poly(β-ketoenamine) TFC membranes for high-efficient multitasking fluid separations.

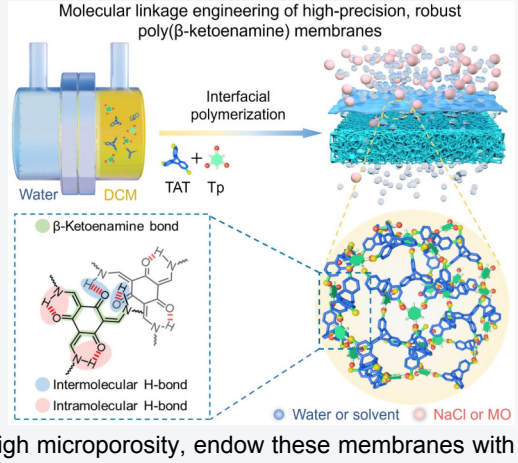

KEYWORDS: poly(β-ketoenamine) membrane, triptycene, interfacial confined growth, thin-film composite, desalination, organic solvent nanofiltration (OSN)

1 Introduction

Fluid separation is a fundamental operation in industries spanning seawater desalination, petrochemicals, and pharmaceuticals [1, 2]. The reliance on traditional energy-intensive thermal processes leads to high energy consumption and substantial emissions of greenhouse gases [3, 4]. This dual environmental cost inevitably intensifies the greenhouse effect and causes considerable ecological damage [5]. Endowed with the inherent high energy efficiency and environmental compatibility, membrane-based separations have emerged as a promising alternative to thermally driven separation processes [6, 7]. In specific, membrane technologies generally operate without requiring phase changes, enabling them to conserve an estimated 90% of energy and substantially reduce carbon emissions [8, 9]. This inherent efficiency is further coupled with high separation selectivity, which relies on size exclusion and

Received: November 13, 2025; **Revised:** December 10, 2025
Accepted: December 29, 2025

✉Address correspondence to Miaomiao Tian, tianmiaomiao@zzu.edu.cn; Junyong Zhu, zhujunyong@zzu.edu.cn

specific interactions with target solutes, validating their extensive applications diverse areas like water treatment and organic solvent nanofiltration (OSN) [10–12].

Thin-film composite (TFC) membranes synthesized via interfacial polymerization, primarily from polyamide, have been crucial in advancing reverse osmosis (RO) for seawater desalination [13]. However, the rapid, irreversible polymerization frequently yields a high-crosslinked polyamide film with limited free volume, which prevents the fabricated membranes from surpassing the permeability–selectivity trade-off [14–16]. Their application in alternative separations like OSN is additionally limited by their low microporosity, insufficient anti-swelling capability, and high mass transfer resistance for low-polarity solvents [17]. In contrast, polyimine-based membranes, exhibiting reduced polarity due to the absence of carbonyl oxygen moieties (C=O), have large potential for fluid separations such as water treatment and OSN [18, 19]. Recently, Liu et al. [20] pioneered the fabrication of microporous polyimine membranes using rational monomer design, achieving a breakthrough in crude oil fractionation. Nevertheless, the inherent rotational flexibility of the imine bond often induces structural reconfiguration and pore swelling upon exposure to harsh solvents, leading to compromised stability and performance [21, 22].

In contrast to imine bonds, poly(β-ketoenamine) is a highly efficient and stable covalent linkage derived from the condensation of β-ketoaldehyde and amine monomers [23]. The formation proceeds in two consecutive stages: (i) Schiff base reaction based on nucleophilic addition, leading to an unstable hydroxyl intermediate, which subsequently dehydrates to yield an imine bond; (ii) keto–enol tautomerism in which a phenolic hydroxyl group acts as an intrinsic proton source, spontaneously transferring a proton to the imine nitrogen, inducing double-bond migration, and thus forming the thermodynamically stable β-ketoenamine configuration [24, 25]. Additionally, it exhibits a unique capacity to form robust intramolecular hydrogen bonding between N–H and adjacent C=O groups, which are further reinforced by intermolecular hydrogen bonding between adjacent polymer chains [26, 27]. These strong hydrogen-bonding interactions, coupled with enhanced π–π conjugation, impart a rigid framework architecture that grants improved hydrolytic stability and solvent resistance [28, 29]. In this context, the rational design of poly(β-ketoenamine) linkages within the selective film holds promise for producing solvent-resistant TFC membranes capable of reliable operation across diverse environments.

To facilitate broader utilization of membrane technologies, highly permeable membranes are requisite for processing high-volume fluid efficiently over a feasible time frame using an applicable membrane area [30]. An efficacious strategy lies in molecular-level engineering of the polymeric membranes to provide enhanced interconnected microporosity [31]. The key to constructing these high-microporosity membranes largely relies on the utilization of 3D, contorted, and shape-persistent monomers [32]. This structural approach effectively suppresses the dense packing of polymer chains, which in turn facilitates the formation of abundant and persistent microporous channels for facilitated molecular transport [33]. To date, several 3D contorted monomers, such as phenolphthalein and its analogs [34], 5,5′,6,6′-tetrahydroxy-3,3,3′,3′-tetramethylspirobisindane (TTSBI) [35], Tröger's base diamine (TBDA) [36], and triptycene-based acylchloride [13], have been successfully deployed for the fabrication of polyamide/polyester TFC membranes. These resultant membranes exhibited improved microporosity and favored structural stability, consequently yielding good OSN performance. However, their use in constructing precisely tailored nanochannels for desalination membranes remains challenging, a limitation directly attributable to rapid and uncontrolled polymerization using high-reactive monomers. This synthetic constraint significantly impedes the development and utilization of these contorted molecular architectures in RO membrane technology.

To this end, we introduce a molecular linkage engineering strategy for the precision synthesis of highly microporous poly(β-ketoenamine) membranes, employing 2,6,14-triaminotriptycene (TAT) and 1,3,5-triformylphloroglucinol (Tp) as promising precursors. This strategic design offers two distinct advantages: (i) The β-ketoenamine linkage, substituting conventional amide or imine bonds, grants access to a tunable pore architecture while preserving high physicochemical stability; (ii) the introduction of the shape-persistent, three-dimensionally contorted triptycene moiety—featuring a rigid paddle-wheel configuration—enables the formation of interconnected, ordered nanoporous channels, concurrently maximizing the free volume within the polymeric network. The moderate interfacial Schiff reaction and subsequent keto–enol tautomerism promotes defect self-correction and the generation of regionally ordered region within the β-ketoenamine nanofilms. The integration of this self-correcting linkage with shape-persistent building blocks furnishes TFC membranes with high surface area, interconnected microporosity, and exceptional structural stability. These combined features confer superior separation efficiency across both water desalination and OSN applications. Ultimately, this work highlights the synergy between the robust molecular linkage and the precisely engineered microporosity of poly(β-ketoenamine) membranes for multipurpose fluid separations.

2 Results and discussion

2.1 Synthesis of Tp-TAT membranes

The contorted, shape-persistent amine monomer (TAT) was synthesized through the sequential nitration of the triptycene followed by a reduction reaction (Fig. S1 in the Electronic Supplementary Material (ESM)). The chemical integrity of TAT molecules was conclusively verified using ^{1}H nuclear magnetic resonance (NMR) and ^{13}C NMR spectrum and mass spectrometry, confirming its successful synthesis as previously reported (Figs. S2–S6 in the ESM) [37]. This crucial amine functionalization enables the subsequent fabrication of poly(β-ketoenamine) TFC membranes via a Schiff-base reaction with Tp linkers and keto–enol tautomerism (Fig. 1(a)). However, a potential challenge arises from the insolubility of TAT units in water due to the presence of multiple nonpolar aromatic rings. To circumvent this, we employed a co-dissolution strategy by positioning both TAT and Tp molecules within an organic phase (dichloromethane, DCM). On this basis, poly(β-ketoenamine) TFC membranes were synthesized *in situ* on a Kevlar support using catalysis-free interfacial confined growth in a two-chamber diffusion cell (Figs. S7 and S8 in the ESM). The assembly involved orienting the top surface of the Kevlar hydrogel towards the DCM phase containing the monomers, while the other chamber was filled with deionized water (Fig. 1(a)). The hydrogel support thus functioned as a reaction scaffold, providing the essential conditions for the

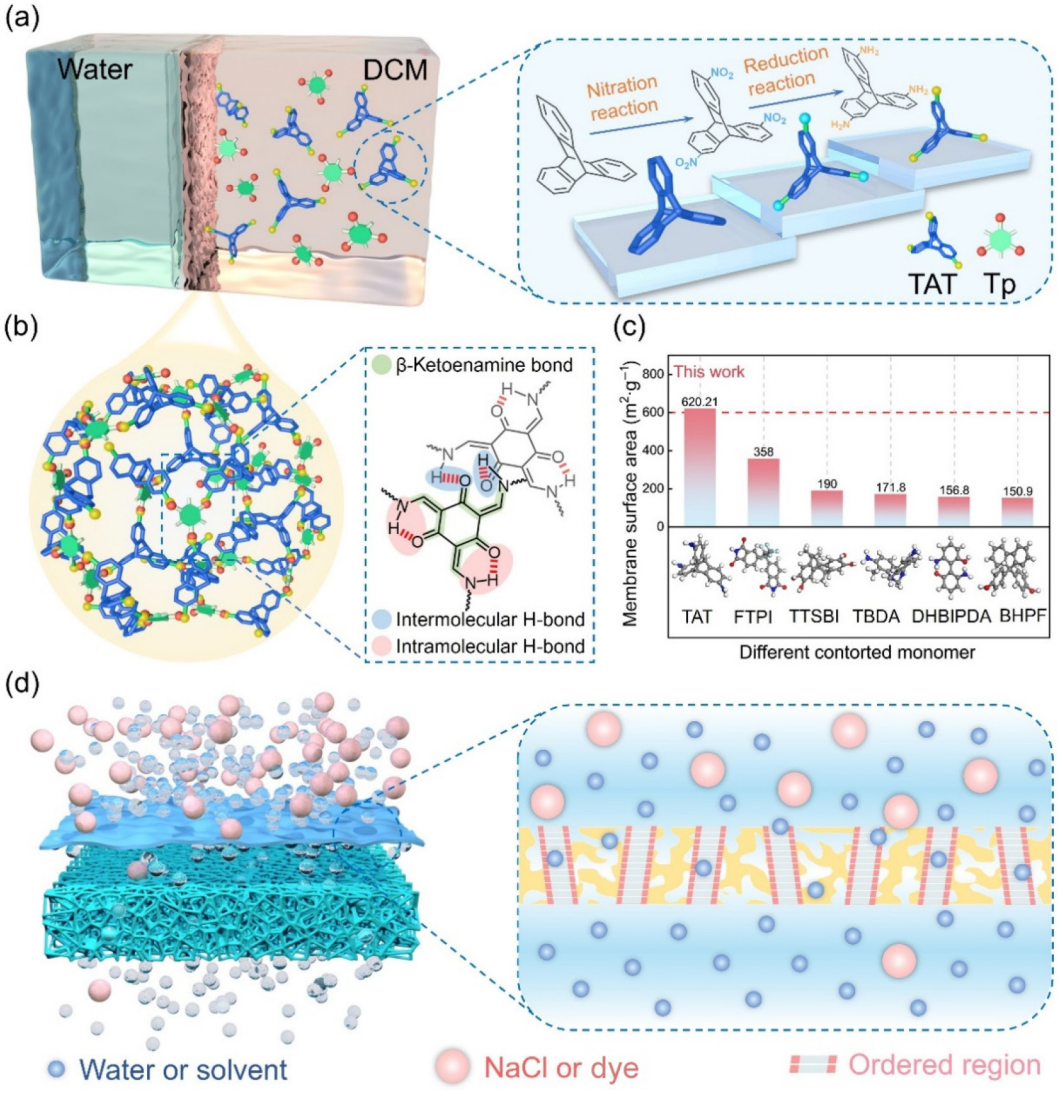

Figure 1 Design, fabrication procedure, and desalination performance of Tp-TAT membranes. (a) Synthesis path of TAT and fabrication of Tp-TAT membranes. (b) Microstructure of Tp-TAT membranes. (c) Comparison of specific surface areas between Tp-TAT membranes and polymer membranes formed by other common 3D-contorted monomers. (d) Schematic illustration of the desalination and OSN mechanism in Tp-TAT membranes.

polycondensation of Tp and TAT monomers to yield a TFC membrane. Driven by monomeric lipophilic character and their robust hydrogen-bonding and π–π interaction with the Kevlar hydrogel, the Schiff base polymerization was confined to the Kevlar/DCM interface, resulting in a continuous and dense Tp‑TAT selective layer. In contrast, monomers dissolved freely in the bulk DCM solution, remote from the hydrogel, lacked the essential confined reaction environment. Over time, these monomers only yielded polymeric nuclei or nanoparticles suspended within the solution bulk, evidenced by the turbidity of the DCM phase and the emergence of the Tyndall effect (Fig. S9 in the ESM). The inherent contorted, non-planar configuration of TAT contributes to 3D interpenetrated microporous networks within the Tp-TAT layer, resulting in a substantially enhanced microporosity (Fig. 1(b)) [38]. The internal poly(β-ketoenamine) linkage further stabilizes the structure by promoting the formation of extensive intra- and intermolecular hydrogen bonded networks, thereby conferring high structural persistence and regionally ordered nanochannels (Fig. S10 in the ESM). Notably, the Tp-TAT membrane demonstrated an exceptionally high specific surface area of 620.21 $m^2 \cdot g^{-1}$, substantially surpassing reported values for polymeric membranes fabricated with conventional contorted monomers (Fig. 1(c)) [32, 35, 36, 39, 40]. The synergy of high microporosity and regionally ordered nanochannels in the fabricated Tp-TAT membranes subsequently resulted in a superior rejection of both NaCl and low-molecular-weight dye models (Fig. 1(d)). This performance highlights their high potential for fluid separations, including RO desalination and OSN applications.

2.2 Characterization of Tp_1-TAT_1-12 freestanding nanofilms

Prior to TFC membrane fabrication, freestanding nanofilms (Tp_1-TAT_1-12) were fabricated at a free water/DCM interface to explore their film-forming ability and physicochemical properties. Attenuated total reflection-Fourier transform infrared (ATR-FTIR) spectroscopy (Fig. 2(a)) demonstrated the successful formation of the β-ketoenamine via a Schiff base reaction, characterized by the emergence of new stretching modes: C=C at 1575 cm^{-1} and C–N at 1290 cm^{-1} [41]. Collectively, the disappearance of the N–H

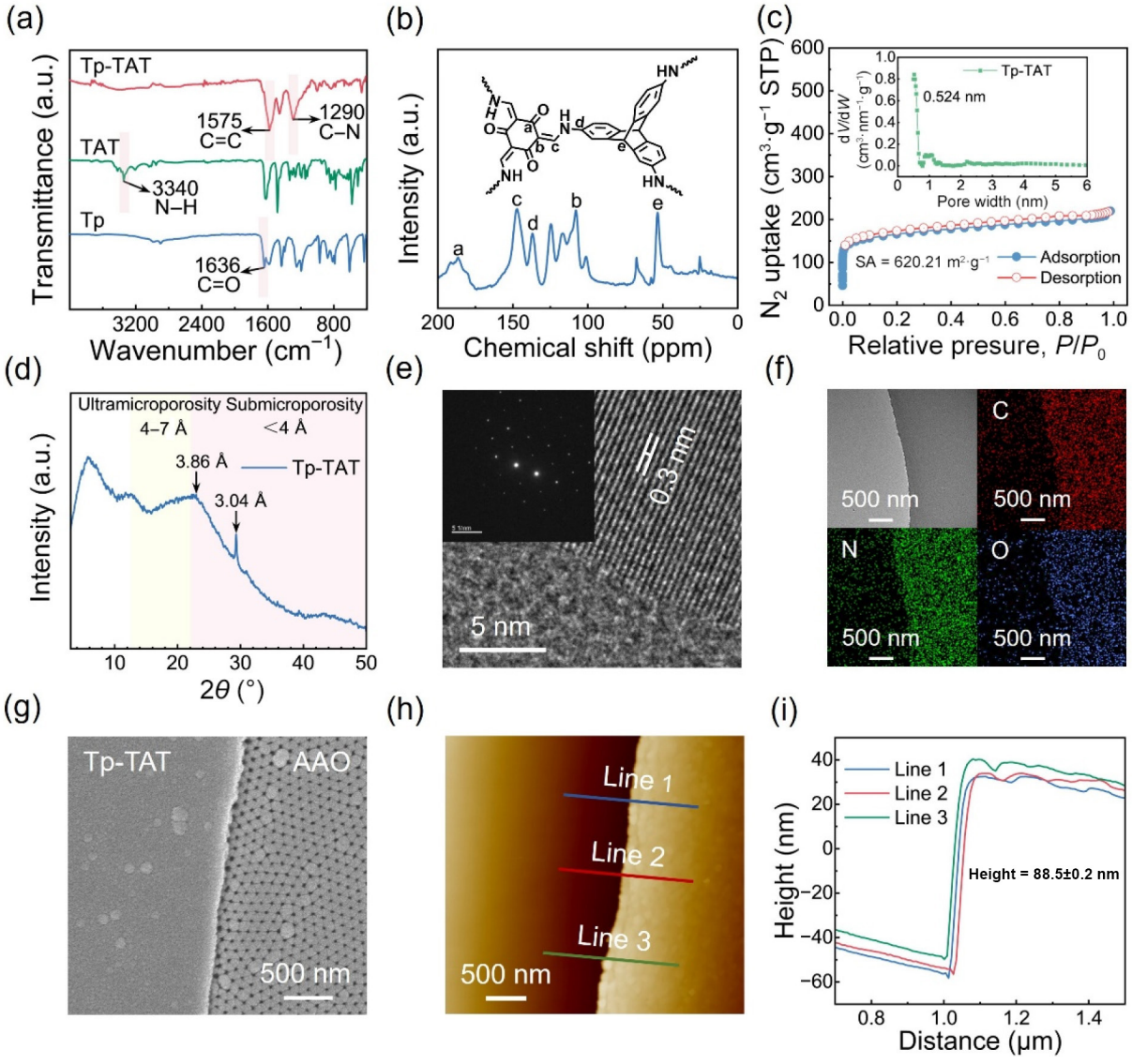

Figure 2 Morphology and characterization of Tp_1-TAT_1-12 freestanding nanofilms prepared via interfacial confined growth. (a) ATR-FTIR spectra and (b) solid-state ^{13}C NMR spectrum of Tp_1-TAT_1-12 nanofilms. (c) N_2 adsorption isotherms of Tp_1-TAT_1-12 nanofilms measured at 77K. The inset denotes pore size distribution employing the NLDFT modeling. (d) XRD pattern of Tp_1-TAT_1-12 nanofilms. (e) HR-TEM image and SAED pattern (inset) of Tp_1-TAT_1-12 nanofilms. (f) TEM image and element mapping of Tp_1-TAT_1-12 nanofilms. (g) SEM top-view image of Tp_1-TAT_1-12 freestanding nanofilms on porous anodic aluminum oxide (AAO) substrate. (h) AFM image and (i) height profile of Tp_1-TAT_1-12 nanofilms.

stretching vibration (3340 cm^{-1} from TAT) and the C=O characteristic peak (1636 cm^{-1} from Tp) conclusively indicated the complete condensation of the aldehyde and amine monomers. Solid-state ^{13}C NMR spectroscopy further provides critical structural confirmation of the β-ketoenamine linkages within the Tp_1-TAT_1-12 films (Fig. 2(b)). Key characteristic chemical shifts observed at 184 and 108 ppm are assigned to C=O and C=C moieties, respectively [42].

The intrinsic microporous nature of Tp_1-TAT_1-12 nanofilms was clearly manifested in the N_2 adsorption–desorption isotherms (Fig. 2(c)), as evidenced by a type I profile featuring pronounced uptake at low relative pressures [43]. Further quantitative analyses revealed the maximum N_2 adsorption capacity of 219.4 $cm^3 \cdot g^{-1}$ and a Brunauer–Emmett–Teller (BET) specific surface area of 620.21 $m^2 \cdot g^{-1}$. The pore size distribution, calculated from the non-local density functional theory (NLDFT) model, revealed a high degree of uniformity, with an average pore diameter of 0.524 nm. This critical dimension is considerably smaller than the estimated hydrated radius of Na^+ ions (≈ 0.72 nm). These findings suggest that the Tp_1-TAT_1-12 membranes are well-suited for high-efficiency NaCl rejection primarily based on the size exclusion.

X-ray diffraction (XRD) patterns of Tp_1-TAT_1-12 nanofilms (Fig. 2(d)) clearly showed key diffraction peaks at 5.8°, 12.1°, 22.6°, and 29.3°. Deconvolution of the XRD profile demonstrated a crystallinity of 55.8% for the nanofilms [44]. Calculations based on Bragg's law demonstrated that the peaks at 22.6° and 29.3° corresponded to d-spacings of 3.86 and 3.04 Å, respectively, highly indicative of hierarchically microporous architecture of the prepared nanofilms [45]. The microstructure of the Tp_1-TAT_1-12 nanofilm was further probed using high-resolution transmission electron microscopy (HR-TEM, Fig. 2(e)), which revealed locally ordered regions with lattice fringe spacings of approximately

0.3 nm. Concurrently, the selected-area electron diffraction (SAED) pattern was manifested as a series of distinctly arranged bright spots in the ordered regions, confirming the high electron scattering efficiency and the polymer crystalline nature of Tp_1-TAT_1-12 nanofilm [46]. Collectively, these results established a locally ordered microstructure within the Tp_1-TAT_1-12 nanofilm, which arises from the robust hydrogen bonding and π–π conjugation that drives the ordered packing of the poly(β-ketoenamine) chains. Morphological analyses of the nanofilms, using both TEM (Fig. 2(f)) and scanning electron microscopy (SEM) images (Fig. 2(g)), revealed their continuous, and defect-free structural integrity. Energy dispersive X-ray spectroscopy (EDS) elemental mapping showed the uniform spatial distribution of C, N, and O within the nanofilms, highlighting their compositional homogeneity. Atomic force microscopy (AFM) characterization further indicated a relatively smooth surface of the freestanding nanofilm, which exhibited an approximate thickness of 88.5 nm (Figs. 2(h) and 2(i)).

2.3 Characterization and desalination performance of Tp-TAT membranes

Building on the success of freestanding nanofilm synthesis, we investigated the *in-situ* fabrication of Tp-TAT composite membranes directly on Kevlar hydrogel substrates. Morphological assessment via SEM (Fig. 3(a)) demonstrated that the resultant Tp_1-TAT_1-12 exhibited superior continuity and defect-free surface compared to the pristine Kevlar, displaying a morphology

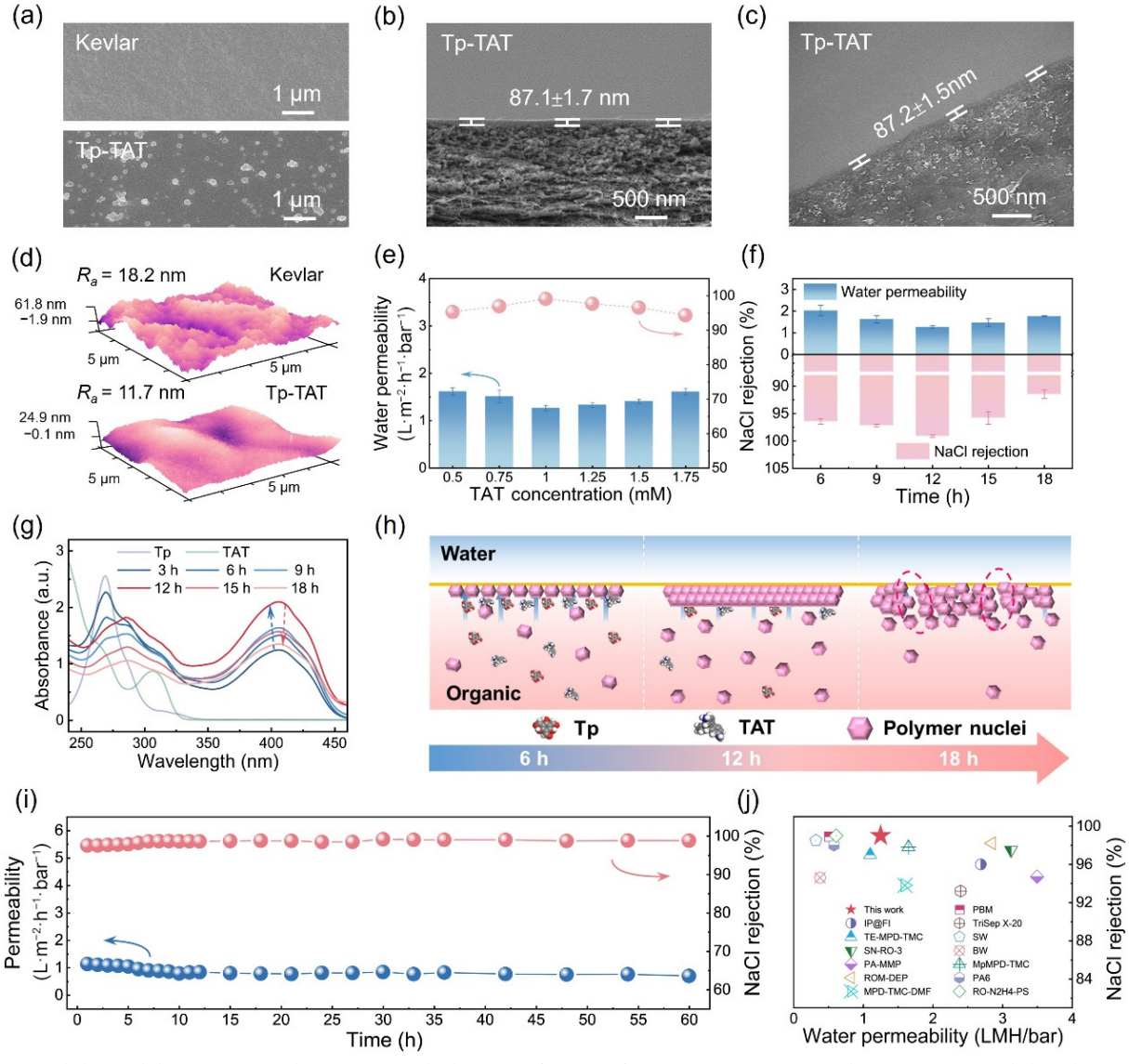

Figure 3 Morphology and characterization and reverse osmosis desalination performance of Tp_1-TAT_1-12 composite membranes. (a) SEM morphological images of Tp_1-TAT_1-12 composite membranes and Kevlar substrates. Cross-sectional (b) SEM image and (c) TEM image of Tp_1-TAT_1-12 membranes. (d) AFM images of Tp_1-TAT_1-12 composite membranes and Kevlar membranes. (e) Desalination performance of Tp_1-TAT_y-12 membranes with different TAT concentrations (Tp concentration remained at 1 mM and the reaction time was 12 h). (f) Water permeability and NaCl rejection of Tp_1-TAT_1-z membranes with different reaction time). (g) UV–vis absorption spectra of oligomer with the progress of the reaction in DCM (the reaction time is from 0 to 18 h). (h) Illustration of molecular linkage engineering approach for membranes formation. (i) Long-term operational stability performance of Tp_1-TAT_1-12 membranes. (j) Desalination performance of Tp_1-TAT_1-12 membranes in comparison with the recently reported RO membranes [14–16, 47–54]. $L{\cdot}m^{-2}{\cdot}h^{-1}{\cdot}bar^{-1}$ stands for liter per square meter per hour per bar. The feeding was 2 $g{\cdot}L^{-1}$ NaCl solution and the operating pressure was 15 bar.

dominated by numerous particulate features. During the synthesis process, the hydrogel support functioned as a reaction carrier, enabling the Tp and TAT monomers to undergo nucleation at its surface and subsequently grow into a continuous layer. Initially, a multitude of discrete nucleation sites formed on the Kevlar surface. These sites exhibited differential growth rates due to the heterogeneous diffusion of monomers from the bulk phases to the interface, yielding a distinctly granular morphology [18, 19]. This pronounced granular texture on the membrane surface became progressively more evident as the reaction time increased. The β-ketoenamine-linked surface layer was confirmed using ATR-FTIR spectroscopy (Fig. S11 in the ESM), which showed characteristic spectral shifts: the appearance of C=C and C–N stretching vibrations coinciding with the disappearance of the N–H and C=O bands. Cross-sectional SEM and TEM images (Figs. 3(b) and 3(c)) revealed that the Tp_1-TAT_1-12 selective layer thickness was approximately 87 nm, consistent with the freestanding nanofilms. This thickness consistency confirms that the Kevlar hydrogel substrate minimally influences the polymerization and assembly of Tp and TAT monomers from the DCM phase, maintaining the integrity of the original fabrication strategy. Additionally, AFM analysis (Fig. 3(d)) demonstrated a distinctly smoother surface topography for the composite membrane, with an average surface roughness (R_a) of 11.7 nm, significantly lower than that of the Kevlar substrate (R_a = 18.2 nm).

X-ray photoelectron spectroscopy (XPS) survey spectra (Fig. S12 in the ESM) revealed discernible differences in the elemental composition. Subsequent deconvolution of the high-resolution C 1s, N 1s, and O 1s spectra (Figs. S13 and S14 in the ESM) identified characteristic peaks for C=C, C=O and C–N bonds. These findings provide further evidence for the successful formation and presence of the β-ketoenamine structure within the surface Tp_1-TAT_1-12 layer [55]. Zeta potential analyses (Fig. S15 in the ESM) demonstrated a weakened surface electronegativity on the Tp_1-TAT_1-12 membranes compared with pristine Kevlar, which is primarily due to the lower electronegativity of β-ketoenamine compared to that of residual carboxyl and polyamide from the Kevlar hydrogel surface. The pore characteristics of Tp_1-TAT_1-12 membranes in aqueous environments were determined by measuring the rejection of neutral solutes with different molecular weights (Fig. S16 and Table S1 in the ESM) [56]. This established a molecular weight cutoff (MWCO) of 90.4 Da, which translates to a pore diameter of 0.43 nm with a narrow distribution. The excellent agreement of this result with BET-derived pore dimensions strongly suggests their high potential for water desalination based on a size-exclusion mechanism.

The desalination performance of Tp_x-TAT_y-z membranes, synthesized with varying monomers concentrations (x, y mM) and reaction time (z h), was evaluated using low-pressure RO with a 2 g·L^{-1} NaCl feed solution. By maintaining a constant Tp concentration (1 mM) and reaction time (12 h), the water permeability of the Tp_1-TAT_y-12 membranes exhibited a distinct V-shaped correlation with increasing TAT concentration (from 0.5 to 1.75 mM). Notably, NaCl rejection peaked at a maximum of 99.1% at the optimal TAT concentration of 1 mM (Fig. 3(e)). Increasing the TAT concentration from 0.5 to 1 mM resulted in the greater consumption of aldehyde groups, which promoted the formation of more β-ketoenamine linkages. This tendency favors the development of a more compact selective layer morphology, consequently leading to enhanced rejections. Conversely, when the TAT concentration exceeded 1 mM, the abundance of amino reaction sites promoted over-reaction, which introduced structural defects into the selective layer and consequently compromised the desalination efficiency [57]. The performance trend observed was validated by similar results obtained when varying the Tp concentration at a constant TAT concentration of 1 mM (Fig. S17 in the ESM). SEM characterization of Tp_x-TAT_y-12 membranes showed polymer particle deposition on all surfaces, with particle density and/or size increasing at higher monomer loads (Figs. S18 and S19 in the ESM). Despite these morphological differences, AFM analysis demonstrated that the surface roughness R_a was consistently low, confined to a narrow range of 10–15 nm (Figs. S20 and S21 in the ESM). Importantly, comprehensive performance evaluation (Fig. S22 and S23 in the ESM) unequivocally showed that only membranes fabricated with a TAT-to-Tp stoichiometry near 1:1 achieved a consistently superior desalination efficiency.

Figure 3(f) illustrates a non-monotonic correlation between reaction time and the desalination performance (NaCl rejection vs. water permeability) of Tp_1-TAT_1-z membranes. In specific, extending the reaction duration from 6 to 12 h resulted in a boosted NaCl rejection at the compromise of water permeability; however, further extension of the time reversed this trade-off. This complex phenomenon was elucidated by detailing the underlying membrane formation mechanism, which was studied using ultraviolet–visible (UV–vis) spectroscopy of the DCM solution coupled with morphological characterization. During the interfacial growth (molecular linkage) at the Kevlar/DCM boundary, a secondary homogeneous nucleation process simultaneously took place in the bulk DCM. The generation of polymer nuclei in the bulk was confirmed via the distinct absorption maximum observed at 413 nm in the UV–vis spectrum. As demonstrated in Fig. 3(g) and Fig. S8 in the ESM, the increased turbidity of the DCM phase aligned kinetically with the rise in the 413 nm absorption peak, indicating that this bulk nucleation process peaked after 12 h of reaction. Figure 3(h) presents the proposed film formation mechanism as a function of reaction time. Extending the reaction duration promoted a more complete Schiff base reaction, resulting in a continuous and defect-free selective layer and the consequent improvement in salt rejection [58]. However, further prolonging the reaction duration over 12 h would cause the overgrowth and random arrangement of polymer chains, thus forming interfacial non-selective defects that markedly compromise the NaCl rejection. SEM and AFM images (Figs. S24 and S25 in the ESM) further confirmed this microstructural change, showing a continual increase in surface particle density and roughness.

The resultant Tp_1-TAT_1-12 membranes demonstrated exceptional long-term operational stability, maintaining stable salt permeability and rejection throughout a 60-h continuous test (Fig. 3(i)). Thermogravimetric analysis (TGA, Fig. S26 in the ESM) revealed that Tp_1-TAT_1-12 membranes decomposed at approximately 400 °C. This exceptional thermal stability primarily stems from the rigid TAT architecture and the strong intermolecular forces (H-bonding and π–π conjugation) within the poly(β-ketoenamine) networks. A performance comparison (Fig. 3(j), Table S2 in the ESM) further established that our fabricated Tp_1-TAT_1-12 membranes possessed competitive advantages in RO desalination relative to other reported state-of-the-art membranes.

Furthermore, we additionally utilized ethyl acetate (EA)—another solvent exhibiting excellent monomer solubility—to

fabricate Tp-TAT membranes using identical optimal conditions. Following desalination performance evaluation, the Tp-TAT-EA membranes exhibited a comparably high desalination performance (Table S3 in the ESM). This result confirms that the molecular linkage engineering strategy is applicable to various organic solvents, provided they offer sufficient solubility for these monomers.

2.4 TAT-based membranes (TAT-M) fabricated using similar aldehyde monomers

To validate the superior structural design of the poly(β-ketoenamine) architecture, we employed molecular linkage engineering to synthesize TFC membranes using TAT with a series of aldehyde monomers featuring different hydroxyl contents, including Tp, 2,4-dihydroxybenzene-1,3,5-tricarbaldehyde (DHTA), 2-hydroxybenzene-1,3,5-tricarbaldehyde (HTA) and 1,3,5-triformylbenzene (TFB). The resulting Tp-TAT, DHTA-TAT, HTA-TAT, and TFB-TAT membranes exhibited distinct morphological and structural characteristics (Figs. 4(a) and 4(b)). ATR-FTIR analyses (Fig. 4(c)) confirmed the presence of hydroxyl groups in DHTA-TAT and HTA-TAT membranes via a stretching vibration at 3665 cm^{-1}, a feature absent in the Tp-TAT spectrum (Fig. 2(a)). Both HTA-TAT and TFB-TAT membranes showed pronounced C=N stretching vibration at 1688 cm^{-1}, indicative of imine bond formation. In contrast, the DHTA-TAT membrane exhibited C=C and C–N stretching vibrations at 1574 and 1296 cm^{-1}, respectively, consistent with those observed in Tp-TAT. Solid-state ^{13}C NMR results (Figs. 2(b) and 4(d) and Fig. S27 in the ESM) demonstrated a strong spectroscopic resemblance between the DHTA-TAT and Tp-TAT structures, both characteristic of poly(β-ketoenamine) linkages. Specifically, both spectra featured characteristic resonances for C=O (184 ppm) and C=C (108 ppm), along with an additional C=N resonance at 145 ppm [42]. In contrast, the spectra of HTA-TAT and TFB-TAT exhibited a

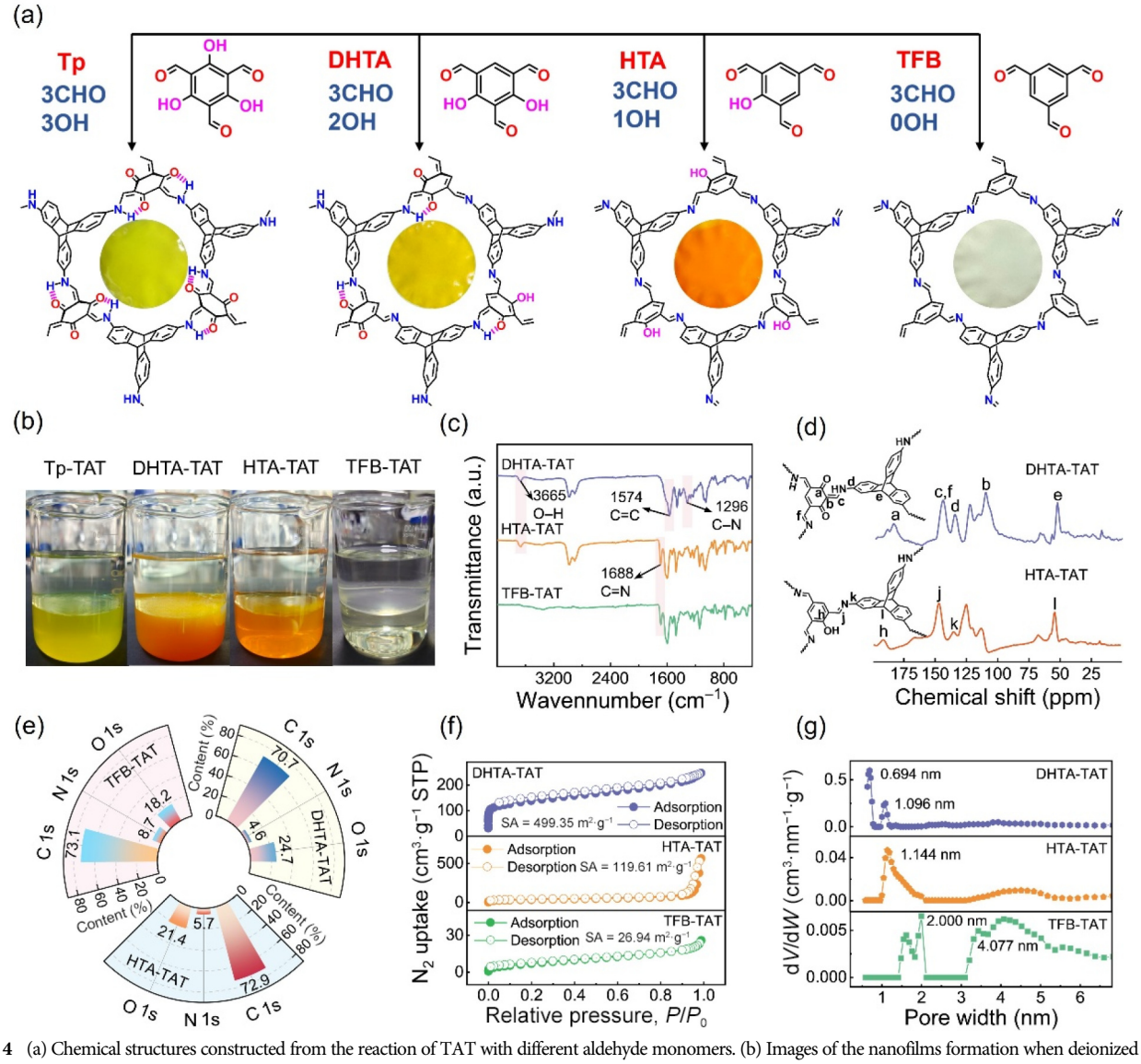

Figure 4 (a) Chemical structures constructed from the reaction of TAT with different aldehyde monomers. (b) Images of the nanofilms formation when deionized water was added to different oligomer precursor DCM solutions, respectively, for 12 h. (c) ATR-FTIR spectra, (d) solid-state ^{13}C NMR spectra and (e) XPS results of different membranes. (f) N_2 adsorption isotherms of different membranes measured at 77 K. (g) Pore size distributions of DHTA-TAT membranes and HTA-TAT membranes calculated by NLDFT modeling. The pore size distributions of TFB-TAT membranes were calculated by BJH method. The concentration of TAT was 1 mM; all aldehyde monomers had the same concentration of 1 mM; the reaction time was 12 h.

simplified profile, displaying only one characteristic C=N peak at 146 ppm. This single peak is the definitive spectroscopic evidence for their formation as polyimine membranes.

Furthermore, the XPS survey spectrum confirmed distinct elemental distributions across the DHTA-TAT, HTA-TAT, and TFB-TAT membranes, which aligns with the varying content of hydroxyl groups in their respective aldehyde monomers (Fig. 4(e)). High-resolution deconvoluted XPS spectra (Figs. S28–S30 in the ESM) clearly evince a structural difference: DHTA-TAT surface layers had both characteristic β-ketoenamine structures and imine bonds, whereas HTA-TAT and TFB-TAT ones were predominantly composed of imine linkages [28, 59]. Based on these results, we conclude the following: i) β-Ketoenamine linkages of the Tp-TAT are attributed to the high symmetry of Tp linkers—featuring three aldehyde and three hydroxyl groups. This facilitates the formation of robust intramolecular six-membered hydrogen-bonded rings upon condensation with TAT, thereby establishing an irreversible polymeric framework. ii) DHTA-TAT membranes exhibit a dynamic tautomeric equilibrium between β-ketoenamine and imine linkages [60]. The stronger β-ketoenamine signals suggest that DHTA-TAT adopts a structural morphology analogous to Tp-TAT.

XRD analysis (Fig. S31 in the ESM) of DHTA-TAT films exhibited characteristic diffraction peaks at 5.8° and 22.6°; HTA-TAT and TFB-TAT showed similar, poorly defined patterns. Peak deconvolution (Fig. S32 in the ESM) quantified a low crystallinity of 30.65% for DHTA-TAT films, while HTA-TAT and TFB-TAT exhibited predominantly amorphous structure. This crystallinity variation is likely dictated by the degree of β-ketoenamine formation. The overall lack of sharp peaks is attributed to the asymmetric and distorted conformation of TAT monomers, intrinsically impeding the growth of highly ordered polymeric frameworks [38]. Interestingly, the strong intramolecular and intermolecular hydrogen bonds associated with the poly(β-ketoenamine) architecture stabilize the chains, leading to improved structural ordering [27]. The fully developed β-ketoenamine configuration thus endows Tp-TAT membranes with the highest crystallinity. The reduced crystallinity observed in DHTA-TAT membranes, relative to Tp-TAT, is probably ascribed to structural reversibility linked to its incomplete tautomeric conversion.

Porosity characteristics of the TAT-M membranes were determined using N_2 adsorption–desorption measurements at 77 K (Figs. 4(f) and 4(g)). BET surface areas were found to be 620.21 (Tp-TAT), 499.35 (DHTA-TAT), 119.61 (HTA-TAT), and 26.94 $m^2 \cdot g^{-1}$ (TFB-TAT), respectively. Although the distorted molecular conformation of TAT inherently produces microporous membranes with a high surface area, the data show a strong correlation: the increase in surface area scales with increasing the hydroxyl content of aldehyde monomers. This enhancement is attributed to the increased density of β-ketoenamine linkages, which facilitates more ordered polymer chain packing. Pore size distributions (PSDs) were derived via NLDFT (DHTA-TAT and HTA-TAT) and Barrett–Joyner–Halenda (BJH) methods (TFB-TAT). DHTA-TAT membranes exhibited a microporous structure with a heterogeneous distribution, centered at 0.694 and 1.096 nm. HTA-TAT membranes were also microporous but had a wider PSD, suggesting limited low-molecular-weight solute rejection. In sharp contrast, TFB-TAT membranes showed a mesoporous structure (predominantly > 2 nm pores), which likely stems from the loosely packed internal framework induced by the TFB linkers.

A systematic evaluation of TAT-M desalination performance (Fig. S33 in the ESM) revealed a clear structure–property relationship: augmenting the hydroxyl group content in the aldehyde monomers remarkably enhanced water permeability while concomitantly reducing the NaCl rejection. As anticipated by our design, the Tp-TAT membranes demonstrated the best comprehensive desalination performance metrics, confirming the efficacy of the selected monomer structure. The film formation rates of these TAT-M membranes were subsequently studied using UV–vis spectroscopy to monitor polymer nuclei formation kinetics (Fig. S34 in the ESM). The apparent rate constant k for polymer nuclei formation was found to be strongly dependent on the aldehyde structure, particularly the number of hydroxyl groups present. The k values decreased in the order: Tp-TAT > DHTA-TAT > HTA-TAT > TFB-TAT, demonstrating that a larger portion of hydroxyl groups facilitated the formation of TAT-M membranes [61]. The resulting highest rate of the Tp-TAT membranes produced denser crosslinked ultra-microporous membranes, accounting for the exceptional NaCl rejection of Tp-TAT membranes. Furthermore, SEM and AFM images (Figs. S35 and S36 in the ESM) of the DHTA-TAT, HTA-TAT, and TFB-TAT membranes revealed relatively smooth and defect-free surface morphologies. This suggests that the internal pore nanostructure, and not surface characteristics, is the principal factor that governs differences in rejection performance.

2.5 Simulations of structural changes of TAT-M membranes

The distorted molecular conformation of shape-persistent TAT and the robust β-ketoenamine linkage collectively endowed the TAT-M membranes with enhanced specific surface area and microporosity. The pore architecture of the fabricated membranes was subsequently studied using realistic structural models of the three TAT-M systems. These models were generated via molecular dynamics (MD) simulations using the PACKMOL software [62], and all simulations were conducted with the GROMACS package [63–65] employing the all-atom force field of orthogonal projection to latent structures (OPLS) [66].

The void space analysis, characterizing spatial voids, interconnectivity, and pore size distributions, was performed using a 0.6 Å probe radius. The TAT moiety induced a three-dimensionally distorted architecture in all TAT-M polymers, significantly increasing the internal cavity interconnectivity (Figs. 5(a)–5(c)). Figure S37 in the ESM depicts the interconnected and disconnected voids in the Tp-TAT, DHTA-TAT, and HTA-TAT network structures. The results confirm high porosity characterized by a majority of interconnected voids, supporting the role of the distorted TAT monomer in developing microporosity. When voids were color-mapped based on the maximum insertable probe diameter (Fig. S38 in the ESM), the Tp-TAT membranes displayed the largest void fraction, underscoring the role of the stable β-ketoenamine structure in promoting the optimal microporosity.

As depicted in Fig. 5(d), the fractional free volume (FFV) followed the trend of Tp-TAT > DHTA-TAT > HTA-TAT, which is consistent with the experimental microporosity findings. The pore size distributions of TAT-M membranes based on molecular simulations are presented in Fig. 5(e). The maximum pore radii for Tp-TAT, DHTA-TAT, and HTA-TAT membranes were found to be 4.4, 4.7, and 4.9 Å, respectively (Table S4 in the ESM). These

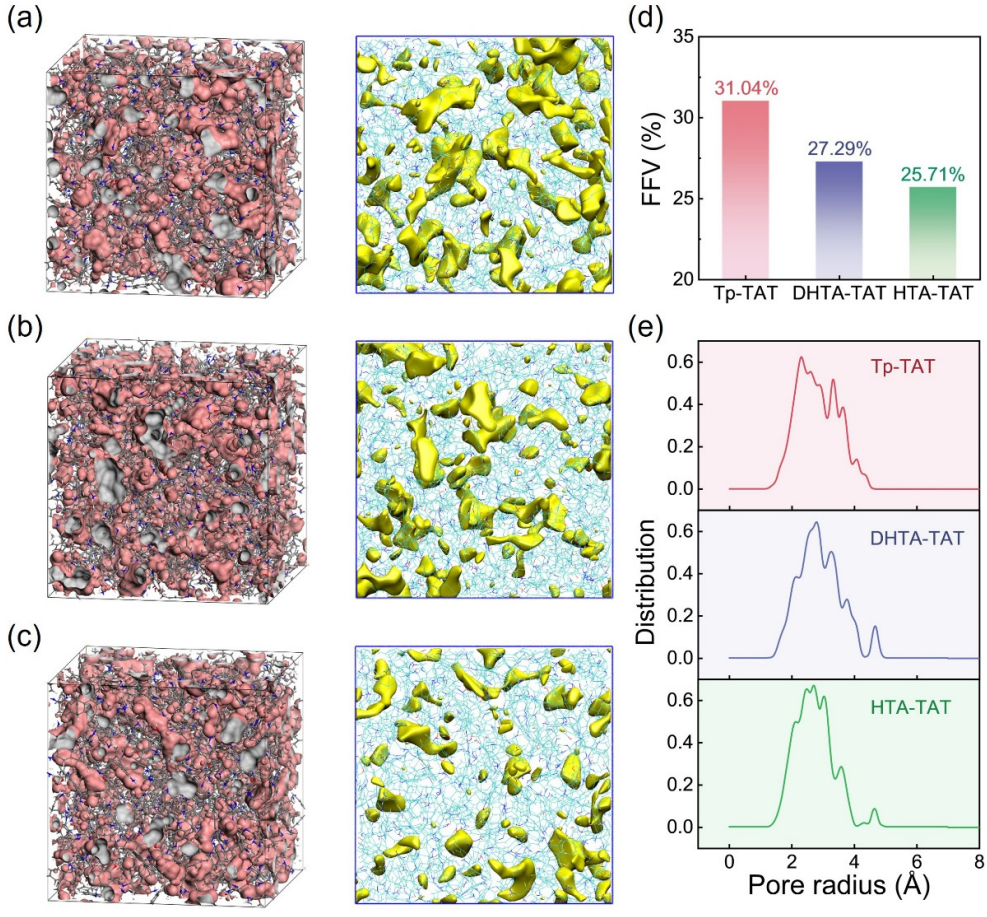

Figure 5 Structural analysis of TAT-M networks models. (a)–(c) Simulations were performed on energy-minimized, three-dimensional amorphous unit cells of the TAT-M networks. The resulting model visualizes the detected voids in pink and their corresponding apertures in gray, employing a probe radius of 0.6 Å. (d) Simulated fractional free volumes (FFVs) of TAT-M membrane systems. (e) Simulated pore size distribution of TAT-M networks system.

values showed good agreement with experimental data, only slightly lower than those obtained experimentally via N_2 adsorption, likely due to the absence of environmental effects in the simulations, leading to an underestimation of actual pore dimensions [11]

2.6 Tp-TAT membranes for organic solvent nanofiltration

The utility of our fabricated Tp_1-TAT_1 membranes extended significantly beyond water desalination, showing large potential for organic solvent nanofiltration (OSN) applications. To optimize their performance, a systematic evaluation was performed to correlate the fabrication reaction time with membrane-based OSN metrics: methanol permeability and methyl orange (MO) rejection. As illustrated in Fig. S39 in the ESM, the Tp_1-TAT_1-6 membrane, synthesized using 6-h reaction time, demonstrated the most favorable combination of high methanol flux and high MO rejection. This optimized membrane was thus chosen for all subsequent analyses, including the critical evaluation of its solvent stability. The stability study, detailed in Fig. S40(a) in the ESM, involved immersing the Tp_1-TAT_1-6 membranes in seven different organic solvents for a period of up to 30 d. The membrane swelling ratios, which were determined by measuring dimensional changes after solvent exposure, are presented in Fig. 6(a). Notably, the swelling remained within a narrow range of 2%–5%, with slightly higher values observed in strongly polar solvents such as DMF and methanol. Crucially, the structural and chemical stability of the membrane was fully preserved. This conclusion was supported by SEM images (Fig. 6(b), Figs. S24(a) and S40(b)–S40(d) in the ESM), which revealed no significant change in surface morphology and the consistent ATR-FTIR spectra (Fig. 6(c)). These findings strongly demonstrated their exceptional anti-swelling characteristics and high solvent resistance.

As revealed in Fig. 6(d), Tp_1-TAT_1-6 membranes exhibited a clear solvent-dependent permeability profile. In specific, the membranes had relatively high permeance toward polar solvents (methanol and acetonitrile) but demonstrated negligible permeance for low-polarity solvents such as n-hexane and toluene. Notably, the pure solvent permeance showed a linear correlation with a predictive mathematical model that integrates key solvent properties, including solubility parameter, viscosity, and molar diameter (Fig. 6(e), Table S5 in the ESM) [67, 68]. Nevertheless, the permeability of DMF and methanol deviated from this established trend. This deviation is primarily attributed to their strong polarity, which triggered more pronounced membrane swelling compared to the effects induced by other solvents.

Following the permeance assessment, the rejection performance of Tp_1-TAT_1-6 membranes was evaluated using organic dyes with different molecular weights (Fig. 6(f)). The resultant membranes exhibited exceptional rejection exceeding 99.2% for all tested species, such as MO, rhodamine B (RhB), acid fuchsin (AF), brilliant blue R (BBR), and rose Bengal (RB), while achieving an outstanding rejection of 99.9% for rose Bengal (Table S6 in the

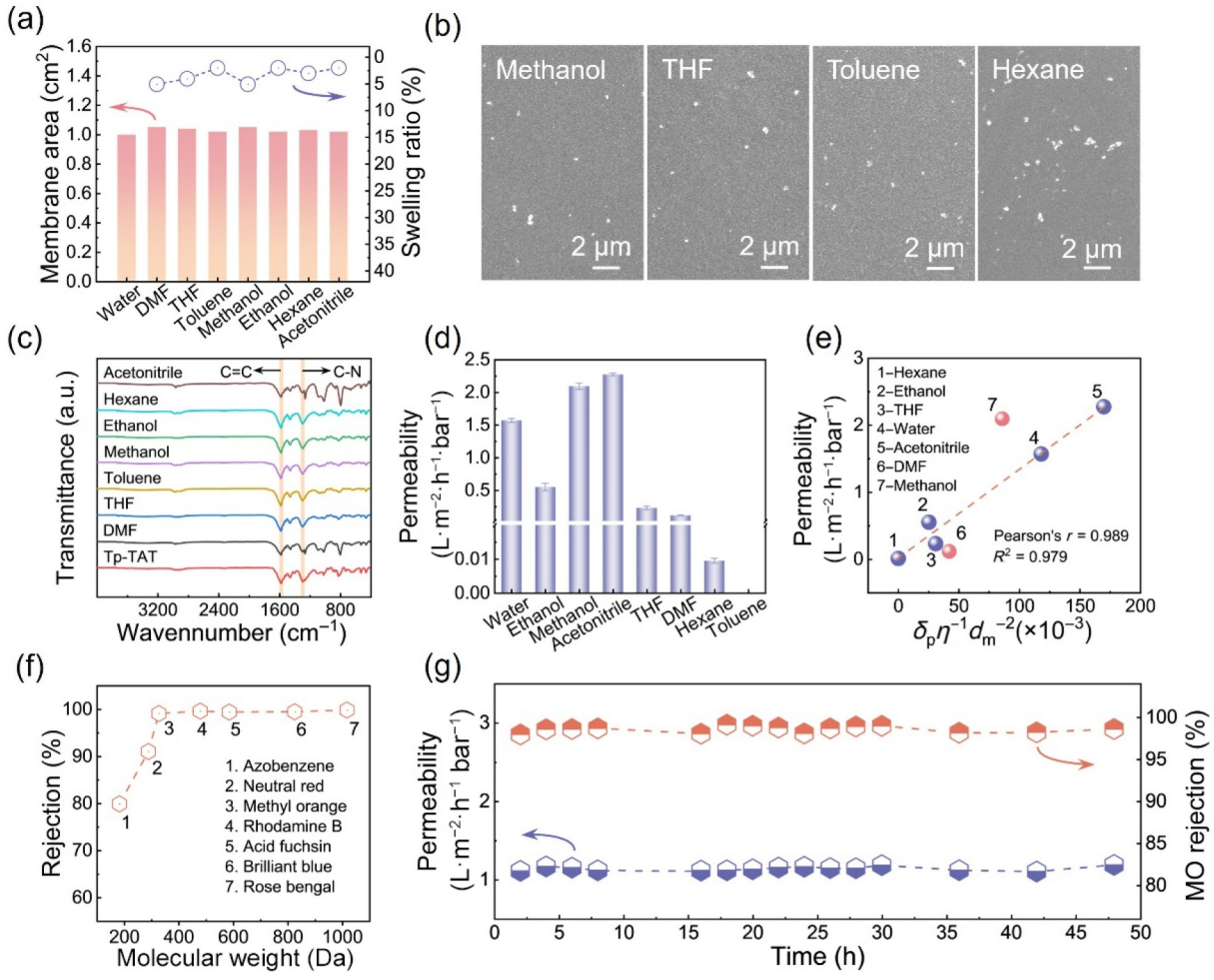

Figure 6 The organic solvent resistance of Tp_1-TAT_1-6 membranes. (a) Swelling ratios, (b) SEM images, and (c) ATR-FTIR spectra of Tp_1-TAT_1-6 membranes after immersion in various organic solvents for 30 days. (d) Different organic solvent permeability of Tp_1-TAT_1-6 membranes. (e) Relationship between organic solvent permeability and its physical properties. (f) Rejection of Tp_1-TAT_1-6 membranes for various dyes in a methanol solution. (g) Long-term stability test of Tp_1-TAT_1-6 membrane for methyl orange methanol solution. All tests were conducted using a dead-end filtration setup at a constant pressure of 10 bar.

ESM). A further significant figure of merit for practical deployment is their excellent operational stability under high-pressure conditions. Tp_1-TAT_1-6 membranes demonstrated pressure-stable performance, as plotted in Fig. S41 in the ESM, and the methanol permeability increased linearly with the applied pressure from 2 to 10 bar. This linear response indicated their structural integrity and stable permeance across varying pressure conditions. This mechanical robustness was primarily attributed to the rigid triptycene-derived framework and the inherent stability of β-ketoenamine linkages. Moreover, during a 48-h continuous filtration of methyl orange/methanol solution, these membranes maintained a constant solution flux and stable methyl orange rejection (Fig. 6(g) and Fig. S42 in the ESM). These results confirmed their exceptional long-term operational stability in organic solvents, validating their suitability for prolonged use.

3 Conclusions

A molecular linkage engineering strategy was successfully presented to fabricate poly(β-ketoenamine) microporous membranes using interfacial confined growth of Tp and TAT monomers. The strategic utilization of the rigid, non-planar TAT conformation engineered an exceptionally high specific surface area, corroborated by molecular simulation, while robust intra- and intermolecular hydrogen bonding endowed the framework with superior structural stability and solvent resistance. This framework stabilization concurrently drove the formation of a locally ordered microstructure that enhanced the microporosity. These Tp-TAT membranes demonstrated potent dual-purpose functionality, achieving a 99.1% NaCl rejection in reverse osmosis desalination and maintaining rejection exceeding 99.2% for dyes (M_W > 327 Da) in organic solvent nanofiltration. Furthermore, a systematic investigation into the effect of hydroxyl group content on aldehyde monomers highlighted the essential role of β-ketoenamine linkages in optimizing membrane structure and performance. This work provides a useful molecular linkage engineering strategy for designing resilient poly(β-ketoenamine) membranes for advancing separation technologies.

4 Methods

Preparation of Kevlar hydrogel membranes: The preparation of the Kevlar hydrogel membranes followed the wet phase inversion method previously established in our work and elsewhere [69]. The process began by dissolving 1.2 g of potassium hydroxide (KOH) in 1.2 g of deionized water. Subsequently, 60 mL of dimethyl sulfoxide

(DMSO) and 1.2 g of Kevlar fibers were sequentially added. The mixture was subjected to continuous stirring for 48 h at ambient temperature to yield a uniform, dark-red solution. Prior to membrane casting, the solution was centrifuged (8000 r/min, 30 min) to effectively eliminate air bubbles and any residual impurities. The homogenized solution was deposited onto a non-woven fabric via tape-casting, employing a knife gap of 250 μm. The coated fabric was instantaneously immersed in a water bath, triggering non-solvent induced phase inversion to yield the Kevlar-hydrogel support membrane (Fig. S11 in the ESM). The resultant hydrogel membrane was stored in deionized water prior to further processing.

Preparation of Tp_1-TAT_1-12 freestanding nanofilms: Free-standing nanofilms were fabricated via interfacial confined growth at the free water/DCM interface. Initially, under ambient temperature, TAT (6.0 mg, 1 mM) and Tp (4.2 mg, 1 mM) were separately dissolved in 10 mL of DCM and ultrasonicated for 5 min to ensure complete monomers dissolution. The two resulting solutions were then mixed and ultrasonicated for additional 30 s to yield the organic precursor solution. The entire solution was poured into a glass culture dish (≈ 5 cm in diameter), followed by careful layering of 20 mL of deionized water to establish a stable water/DCM interface. After a reaction period of 12 h, a continuous freestanding nanofilm was obtained. The as-prepared Tp_1-TAT_1-12 nanofilms were transferred onto silicon wafers, porous anodic aluminum oxide sheets, or copper grids for characterizations.

Preparation of Tp_1-TAT_1-12 membranes: Tp_1-TAT_1-12 membranes were fabricated onto a Kevlar hydrogel substrate using interfacial confined growth within a custom-fabricated diffusion cell. First, TAT (6.0 mg, 1 mM) and Tp (4.2 mg, 1 mM) were individually dissolved in 10 mL of DCM, with 5-min ultrasonication ensuring monomer dissolution. The Kevlar membrane support prepared by cutting it into a circular disc (5 cm diameter), and residual surface moisture was removed via nitrogen purging. This disc was then vertically secured and sealed at the center of the glass diffusion cell (20 mL volume). Subsequently, 20 mL water was introduced into the chamber on the back side of the Kevlar support. The individual TAT and Tp solutions were mixed and ultrasonicated for 30 s to form the organic precursor solution, which was subsequently added into the chamber toward the top surface of the Kevlar substrate. Following a 12-h reaction period at room temperature, the resulting Tp_1-TAT_1-12 membrane was rinsed with DCM to eliminate any unreacted species, and stored in deionized water. An identical protocol was utilized for the preparation of DHTA-TAT, HTA-TAT, and TFB-TAT membranes.

Electronic Supplementary Material: Supplementary material (detailed description of materials, testing and characterization methods, with accompanying figures including the synthetic route of the TAT monomer and its ^{1}H and ^{13}C NMR spectra, characterization and performance data plots for the Kevlar substrate membrane and composite membranes, and simulation data plots; and supplementary tables comprising molecular formulas of various alcohols, comparison of membrane performance with literature data, simulation data, solvent properties, and molecular formulas of various dyes) is available in the online version of this article at https://doi.org/10.26599/NR.2026.94908385.

Data availability

All data needed to support the conclusions in the paper are presented in the manuscript and/or the Electronic Supplementary Material. Additional data related to this paper may be requested from the corresponding author upon request.

Acknowledgements

This work was supported by the National Natural Science Foundation of China (Nos. 92475120 and 52573238), the Outstanding Youth Fund of Henan Scientific Committee (No. 252300421182), and Jiangsu Future Membrane Technology Innovation Center (No. BM2021804). The characterizations were measured in the Center of Advanced Analysis and Computational Science at Zhengzhou University and the National Supercomputing Center in Zhengzhou, respectively.

Declaration of competing interest

All the contributing authors report no conflict of interests in this work.

Author contribution statement

B. Y Z.: investigation, experimental design, methodology, data curation, formal analysis, validation, and writing - original draft. G. S. H.: conceptualization, investigation, validation, and visualization. Y. B. C.: conceptualization, validation, and visualization. M. M. T.: conceptualization, validation, supervision, and writing - review & editing. X. L. C.: methodology, and validation. S.-P. S.: conceptualization, and methodology. J. W. H.: formal analysis, and validation. Y. T. Z.: conceptualization, validation, and formal analysis. B. V. d. B.: conceptualization, validation, and supervision. J. Y. Z.: conceptualization, methodology, supervision, resources, funding acquisition, and writing - review & editing. All the authors have approved the final manuscript.

Use of AI statement

None.

References

[1] Werber, J. R.; Osuji, C. O.; Elimelech, M. Materials for next-generation desalination and water purification membranes. *Nat. Rev. Mater.* **2016**, *1*, 16018.

[2] Koros, W. J.; Zhang, C. Materials for next-generation molecularly selective synthetic membranes. *Nat. Mater.* **2017**, *16*, 289–297.

[3] Liang, B.; He, X.; Hou, J. J.; Li, L. S.; Tang, Z. Y. Membrane separation in organic liquid: Technologies, achievements, and opportunities. *Adv. Mater.* **2019**, *31*, 1806090.

[4] Sholl, D. S.; Lively, R. P. Seven chemical separations to change the world. *Nature* **2016**, *532*, 435–437.

[5] Mathew, T. J.; Narayanan, S.; Jalan, A.; Matthews, L.; Gupta, H.; Billimoria, R.; Pereira, C. S.; Goheen, C.; Tawarmalani, M.; Agrawal, R. Advances in distillation: Significant reductions in energy consumption and carbon dioxide emissions for crude oil separation. *Joule* **2022**, *6*, 2500–2512.

[6] Feng, W. L.; Li, F. P.; Li, J. Q.; Li, Z. Y.; Xu, L.; Guo, H. K.; Li, N. W.; Cao, X. Z.; Fang, C. J.; Zhu, B. K. et al. Asymmetrical polyimide membranes with programmable polymer chain architectures for liquid hydrocarbon fractionation. *Sci. Adv.*, **2025**, *11*, eady3674.

[7] Zhang, A. W.; Mai, Z. H.; Zhu, X.; Song, T. Q.; Yan, X. R.; Hou, J. W.; Zhang, Y. T.; Matsuyama, H.; Van Der Bruggen, B.; Zhu, J. Y. Metal-organic framework quasi-monolayer integrated composite membranes for selective rare-metal separation. *Adv. Funct. Mater.* **2025**, *35*, 2507870.
[8] Gin, D. L.; Noble, R. D. Designing the next generation of chemical separation membranes. *Science* **2011**, *332*, 674–676.
[9] Wang, H. L.; Wang, M. D.; Liang, X.; Yuan, J. Q.; Yang, H.; Wang, S. Y.; Ren, Y. X.; Wu, H.; Pan, F. S.; Jiang, Z. Y. Organic molecular sieve membranes for chemical separations. *Chem. Soc. Rev.* **2021**, *50*, 5468–5516.
[10] Logan, B. E.; Elimelech, M. Membrane-based processes for sustainable power generation using water. *Nature* **2012**, *488*, 313–319.
[11] Yao, A. Y.; Hou, J. J.; Dou, P. J.; Du, J. C.; Sun, Q.; Song, Z. Y.; Liu, L. H.; Guan, J.; Liu, J. T. Microporous polyarylate membranes based on 3D phenolphthalein for molecular sieving. *Sci. Adv.,* **2024**, *10*, eado7687.
[12] Bruno, N. C.; Mathias, R.; Lee, Y. J.; Zhu, G. H.; Ahn, Y. H.; Rangnekar, N. D.; Johnson, J. R.; Hoy, S.; Bechis, I.; Tarzia, A. et al. Solution-processable polytriazoles from spirocyclic monomers for membrane-based hydrocarbon separations. *Nat. Mater.* **2023**, *22*, 1540–1547.
[13] Ali, Z.; Ghanem, B. S.; Wang, Y. G.; Pacheco, F.; Ogieglo, W.; Vovusha, H.; Genduso, G.; Schwingenschlögl, U.; Han, Y.; Pinnau, I. Finely tuned submicroporous thin-film molecular sieve membranes for highly efficient fluid separations. *Adv. Mater.* **2020**, *32*, 2001132.
[14] Popova, A.; Boivin, S.; Shintani, T.; Fujioka, T. Development of high-integrity reverse osmosis membranes for enhanced removal of microorganisms. *Desalination* **2024**, *572*, 117155.
[15] Li, S. L.; Wu, P. F.; Wang, J. T.; Wang, J.; Hu, Y. X. Fabrication of high performance polyamide reverse osmosis membrane from monomer 4-morpholino-m-phenylenediamine and tailoring with zwitterions. *Desalination* **2020**, *473*, 114169.
[16] Wang, Q. H.; Ma, H. Y.; Khan, M.; Hsiao, B. S. Reverse osmosis membrane containing hydrazine as architecture unit. *J. Membr. Sci.* **2024**, *697*, 122502.
[17] Li, S. Y.; Dong, R. J.; Musteata, V. E.; Kim, J.; Rangnekar, N. D.; Johnson, J. R.; Marshall, B. D.; Chisca, S.; Xu, J.; Hoy, S. et al. Hydrophobic polyamide nanofilms provide rapid transport for crude oil separation. *Science* **2022**, *377*, 1555–1561.
[18] Shi, X. S.; Zhang, Z. P.; Yin, C. C.; Zhang, X.; Long, J. H.; Zhang, Z.; Wang, Y. Design of three-dimensional covalent organic framework membranes for fast and robust organic solvent nanofiltration. *Angew. Chem., Int. Ed.* **2022**, *61*, e202207559.
[19] Tiwari, K.; Sarkar, P.; Modak, S.; Singh, H.; Pramanik, S. K.; Karan, S.; Das, A. Large area self-assembled ultrathin polyimine nanofilms formed at the liquid–liquid interface used for molecular separation. *Adv. Mater.* **2020**, *32*, 1905621.
[20] Lee, T. H.; Balcik, M.; Ali, Z.; Joo, T.; Rivera, M. P.; Pinnau, I.; Smith, Z. P. Microporous polyimine membranes for efficient separation of liquid hydrocarbon mixtures. *Science* **2025**, *388*, 839–844.
[21] Li, Y.; Sui, J. F.; Cui, L. S.; Jiang, H. L. Hydrogen bonding regulated flexibility and disorder in hydrazone-linked covalent organic frameworks. *J. Am. Chem. Soc.* **2023**, *145*, 1359–1366.
[22] Kang, C. J.; Zhang, Z. Q.; Wee, V.; Usadi, A. K.; Calabro, D. C.; Baugh, L. S.; Wang, S.; Wang, Y. X.; Zhao, D. Interlayer shifting in two-dimensional covalent organic frameworks. *J. Am. Chem. Soc.* **2020**, *142*, 12995–13002.
[23] Chu, F.; Hai, G. T.; Zhao, D. F.; Liu, S. H.; Hu, Y. Z.; Zhao, G. X.; Peng, B. X.; Wang, G.; Huang, X. B. Regulating keto–enol tautomerism of β-ketoenamine covalent-organic frameworks for photocatalytic oxidative coupling of amines. *ACS Catalysis* **2023**, *13*, 13167–13180.
[24] Zhang, Y. D.; He, P.; Zhang, M. C.; Zhang, J.; He, N. N.; Zou, Y. D.; Fan, Z. Y.; Deng, C.; Li, Y.; Ma, L. J. Mild and subtle synthesis of β-ketoenamine COFs with high crystallinity and controllable solubility guided by a monomer preassembly strategy. *Small* **2024**, *20*, 2407874.
[25] Zhang, Y. Q.; Guo, J.; Han, G.; Bai, Y. P.; Ge, Q. C.; Ma, J.; Lau, C. H.; Shao, L. Molecularly soldered covalent organic frameworks for ultrafast precision sieving. *Sci. Adv.,* **2021**, *7*, eabe8706.
[26] Tang, J. H.; Liao, Y.; Pan, Z. X.; Fang, S. J.; Tang, M. X.; Shao, L.; Han, G. Interface-confined catalytic synthesis of anisotropic covalent organic framework nanofilm for ultrafast molecular sieving. *Adv. Sci.* **2025**, *12*, 2415520.
[27] AbdulHalim, R. G.; Garai, B.; De Vos, J. S.; Borgmans, S.; Gkoura, L.; Varghese, S.; Benyettou, F.; Olson, M. A.; Rogge, S. M. J.; Trabolsi, A. Maximizing porosity and water sorption in covalent organic frameworks via β-ketoenamine linkages. *Small* **2025**, *21*, e08046.
[28] Zhang, J. H.; Li, X. N.; Hu, H. J.; Huang, H. W.; Li, H.; Sun, X. D.; Ma, T. Y. Enhancing photocatalytic performance of covalent organic frameworks via ionic polarization. *Nat. Commun.* **2024**, *15*, 9576.
[29] DeBlase, C. R.; Silberstein, K. E.; Truong, T. T.; Abruña, H. D.; Dichtel, W. R. β-Ketoenamine-linked covalent organic frameworks capable of pseudocapacitive energy storage. *J. Am. Chem. Soc.* **2013**, *135*, 16821–16824.
[30] Lee, T. H.; Balcik, M.; Wu, W. N.; Pinnau, I.; Smith, Z. P. Dual-phase microporous polymer nanofilms by interfacial polymerization for ultrafast molecular separation. *Sci. Adv.,* **2024**, *10*, eadp6666.
[31] Wu, J. L.; Xu, F.; Li, S. M.; Ma, P. W.; Zhang, X. C.; Liu, Q. H.; Fu, R. W.; Wu, D. C. Porous polymers as multifunctional material platforms toward task-specific applications. *Adv. Mater.* **2019**, *31*, 1802922.
[32] Jimenez-Solomon, M. F.; Song, Q. L.; Jelfs, K. E.; Munoz-Ibanez, M.; Livingston, A. G. Polymer nanofilms with enhanced microporosity by interfacial polymerization. *Nat. Mater.* **2016**, *15*, 760–767.
[33] Bai, Y. X.; Liu, B. B.; Li, J. C.; Li, M. H.; Yao, Z.; Dong, L. L.; Rao, D. W.; Zhang, P.; Cao, X. Z.; Villalobos, L. F. et al. Microstructure optimization of bioderived polyester nanofilms for antibiotic desalination via nanofiltration. *Sci. Adv.,* **2023**, *9*, eadg6134.
[34] Yao, A. Y.; Meng, D. J.; Du, J. C.; Yu, B. Z.; Sun, Q.; Dou, P. J.; Guan, J.; Liu, J. T. Ultrathin aromatic polyamide membranes with tunable microporosity for molecular sieving. *Angew. Chem., Int. Ed.* **2025**, *64*, e202506493.
[35] Zhang, P. F.; Li, H. Y.; Veith, G. M.; Dai, S. Soluble porous coordination polymers by mechanochemistry: From metal-containing films/membranes to active catalysts for aerobic oxidation. *Adv. Mater.* **2015**, *27*, 234–239.
[36] Yang, C. L.; Liu, S. Q.; Zhao, Q. Y.; Zhang, X. F.; Wang, Z. G.; Zhang, F.; Jin, J. V-shape Tröger's base-based organic solvent nanofiltration membranes for fast and precise molecular separation. *J. Membr. Sci.* **2024**, *711*, 123227.
[37] Zhang, C.; Chen, C. F. Synthesis and structure of 2,6,14- and 2,7,14-trisubstituted triptycene derivatives. *J. Org. Chem.* **2006**, *71*, 6626–6629.
[38] Alam, A.; Hassan, A.; Das, N. Triptycene-based porous organic network polymers: From synthesis to applications. *Prog. Mater. Sci.* **2026**, *155*, 101528.
[39] Chen, Y. C.; Shi, W. X.; Li, S. L.; Wang, M. F.; Wang, J.; Hao, S.; Gong, G. H.; Ye, C. C.; McKeown, N. B.; Hu, Y. X. Rapid and precise molecular nanofiltration using ultra-thin-film membranes derived from 6,6′-dihydroxy-2,2′-biphenyldiamine. *Adv. Funct. Mater.* **2024**, *34*, 2406430.
[40] Zhang, Q. P.; Wang, Z.; Zhang, Z. W.; Zhai, T. L.; Chen, J. J.; Ma, H.; Tan, B. E.; Zhang, C. Triptycene-based chiral porous polyimides for enantioselective membrane separation. *Angew. Chem., Int. Ed.* **2021**, *133*, 12891–12895.
[41] Hu, G. S.; Zhou, B. Y.; Zhen, Y.; Zhu, J. Y.; Hou, J. W.; Zhang, Y.

T.; Wang, Y.; Van Der Bruggend, B. Covalent organic framework catalytic membranes for durable multitasking water purification. *Chem. Sci.* **2025**, *16*, 18141–18151.
[42] Hassan, A.; Alam, A.; Ansari, M.; Das, N. Hydroxy functionalized triptycene based covalent organic polymers for ultra-high radioactive iodine uptake. *Chem. Eng. J.* **2022**, *427*, 130950.
[43] Ge, L.; Li, J. Q.; Du, G. J.; Sheng, K.; Hou, J. W.; Zhou, B. Y.; Zhang, Y. T.; Van Der Bruggen, B.; Zhu, J. Y. Microporous polyacylhydrazone membranes with 3D interconnected nanochannels for accurate molecular sieving. *Adv. Funct. Mater.* **2025**, *35*, 2504997.
[44] Lu, G.; Shang, W. T.; Ma, X. Y.; Xu, H. Y.; A, H. B.; Sun, J. W.; Li, X. L.; Jia, M. Y.; Lu, S.; Wu, J. et al. Supramolecular nanocrystalline membranes with well-aligned subnanochannels for enhanced reverse osmosis desalination. *Nat. Commun.* **2025**, *16*, 6289.
[45] Ge, L.; Du, G. J.; Song, H. J.; Li, J. Q.; Hou, J. W.; Zhang, Y. T.; Zhu, J. Y. 3D covalent organic network membranes with regionally ordered nanochannels for efficient molecular sieving. *Adv. Sci.* **2025**, *12*, e10911.
[46] Lu, G.; A, H. B.; Zhao, Y. Y.; Zhao, Y.; Xu, H. Y.; Shang, W. T.; Chen, X.; Sun, J. W.; Zhang, H. C.; Wu, J. et al. Nano-confined controllable crystallization in supramolecular polymeric membranes for ultra-selective desalination. *Nat. Commun.* **2025**, *16*, 2284.
[47] Khorshidi, B.; Thundat, T.; Fleck, B. A.; Sadrzadeh, M. A Novel Approach Toward Fabrication of High Performance Thin Film Composite Polyamide Membranes. *Scientific Reports* **2016**, *6*, 22069.
[48] Jiang, Z.; Karan, S.; Livingston, A. G. Water Transport through Ultrathin Polyamide Nanofilms Used for Reverse Osmosis. *Advanced Materials* **2018**, *30*, 1705973.
[49] Gorgojo, P.; Jimenez-Solomon, M. F.; Livingston, A. G. Polyamide thin film composite membranes on cross-linked polyimide supports: Improvement of RO performance via activating solvent. *Desalination* **2014**, *344*, 181-188.
[50] Qi, S.; Fang, W.; Siti, W.; Widjajanti, W.; Hu, X.; Wang, R. Polymersomes-based high-performance reverse osmosis membrane for desalination. *Journal of Membrane Science* **2018**, *555*, 177-184.
[51] Feng, S.; Low, Z.-X.; Liu, S.; Zhang, L.; Zhang, X.; Simon, G. P.; Fang, X.-Y.; Wang, H. Microporous polymer incorporated polyamide membrane for reverse osmosis desalination. *Journal of Membrane Science* **2020**, *610*, 118299.
[52] Qin, Y.; Zhu, Z.; Kang, G.; Yu, H.; Cao, Y. Plasticizer-assisted interfacial polymerization for fabricating advanced reverse osmosis membranes. *Journal of Membrane Science* **2021**, *619*, 118788.
[53] Guan, K.; Fang, S.;Zhou, S.; Fu, W.;Li, Z.; Gonzales, R. R.; Xu, P.;Mai, Z.; Hu, M.; Zhang, P.; Matsuyama, H. Thin film composite membrane with improved permeance for reverse osmosis and organic solvent reverse osmosis. *Journal of Membrane Science* **2023**, *688*, 122104.
[54] Xie, T.; Wang, H.; Chen, K.;Li, F.; Zhao, S.; Sun, H.; Yang, X.; Hou, Y.; Li, P.; Niu, Q. J. High-performance polyethyleneimine based reverse osmosis membrane fabricated via spin-coating technology. *Journal of Membrane Science* **2023**, *668*, 121248.
[55] Sun, Q.; Song, Z. Y.; Du, J. C.; Yao, A. Y.; Liu, L. H.; He, W.; Hassan, S. U.; Guan, J.; Liu, J. T. Covalent organic framework membranes with regulated orientation for monovalent cation sieving. *ACS Nano* **2024**, *18*, 27065–27076.
[56] Li, C.; Zhao, Y. L.; Lai, G. S.; Wang, R. Fabrication of fluorinated polyamide seawater reverse osmosis membrane with enhanced boron removal. *J. Membr. Sci.* **2022**, *662*, 121009.
[57] Liu, H. H.; Liang, L. J.; Tian, F.; Xi, X. G.; Zhang, Y. Q.; Zhang, P.; Cao, X. Z.; Bai, Y. X.; Zhang, C. F.; Dong, L. L. Scalable preparation of ultraselective and highly permeable fully aromatic polyamide nanofiltration membranes for antibiotic desalination. *Angew. Chem., Int. Ed.* **2024**, *63*, e202402509.
[58] Mahato, A. K.; Bag, S.; Sasmal, H. S.; Dey, K.; Giri, I.; Linares-Moreau, M.; Carbonell, C.; Falcaro, P.; Gowd, E. B.; Vijayaraghavan, R. K. et al. Crystallizing sub 10 nm covalent organic framework thin films via interfacial-residual concomitance. *J. Am. Chem. Soc.* **2021**, *143*, 20916–20926.
[59] Fang, L.; Xu, H.; Qiu, S. Y.; Ye, T.; Wang, T. Q.; Shang, J.; Gu, C.; Kitagawa, S.; Li, L. C. Autocatalytic interfacial synthesis of self-standing amide-linked covalent organic framework membranes. *Angew. Chem., Int. Ed.* **2025**, *64*, e202423220.
[60] Traxler, M.; Gisbertz, S.; Pachfule, P.; Schmidt, J.; Roeser, J.; Reischauer, S.; Rabeah, J.; Pieber, B.; Thomas, A. Acridine-functionalized covalent organic frameworks (COFs) as photocatalysts for metallaphotocatalytic C−N cross-coupling. *Angew. Chem., Int. Ed.* **2022**, *61*, e202117738.
[61] Pang, X.; Shi, B. B.; Liu, Y. W.; Li, Y. L.; Zhang, Y. F.; Wang, T. T.; Xu, S. T.; Wang, X. Y.; Liu, Z. W.; Xing, N. et al. Phosphorylated covalent organic framework membranes toward ultrafast single lithium-ion transport. *Adv. Mater.* **2024**, *36*, 2413022.
[62] Martínez, L.; Andrade, R.; Birgin, E. G.; Martínez, J. M. PACKMOL: A package for building initial configurations for molecular dynamics simulations. *J. Comput. Chem.* **2009**, *30*, 2157–2164.
[63] Pronk, S.; Páll, S.; Schulz, R.; Larsson, P.; Bjelkmar, P.; Apostolov, R.; Shirts, M. R.; Smith, J. C.; Kasson, P. M.; Van Der Spoel, D. et al. GROMACS 4.5: a high-throughput and highly parallel open source molecular simulation toolkit. *Bioinformatics* **2013**, *29*, 845–854.
[64] Hess, B.; Kutzner, C.; Van Der Spoel, D.; Lindahl, E. GROMACS 4: Algorithms for highly efficient, load-balanced, and scalable molecular simulation. *J. Chem. Theory Comput.* **2008**, *4*, 435–447.
[65] Abraham, M. J.; Murtola, T.; Schulz, R.; Páll, S.; Smith, J. C.; Hess, B.; Lindahl, E. GROMACS: High performance molecular simulations through multi-level parallelism from laptops to supercomputers. *SoftwareX* **2015**, *1–2*, 19–25.
[66] Jorgensen, W. L.; Maxwell, D. S.; Tirado-Rives, J. Development and testing of the OPLS all-atom force field on conformational energetics and properties of organic liquids. *J. Am. Chem. Soc.* **1996**, *118*, 11225–11236.
[67] Yang, H.; Zhang, H. Y.; Kang, C. J.; Ji, C. Q.; Shi, D. C.; Zhao, D. Solvent-responsive covalent organic framework membranes for precise and tunable molecular sieving. *Sci. Adv.*, **2024**, *10*, eads0260.
[68] Fu, P.; Xin, J. H.; Li, W. L.; Lin, W. T.; Zhang, Z. L.; Luo, X. W.; Liu, C.; Chen, J. R. T.; Su, R. K.; Zhang, S. Y. et al. Ultraselective amino-phenolic nanofiltration membranes via enzyme-mediated decoupling of diffusion and reaction. *ACS Nano* **2025**, *19*, 31000–31009.
[69] Zhou, B. Y.; Wang, Y. F.; Tian, M. M.; Cao, X. L.; Han, L.; Sun, S. P.; Zhang, Y. T.; Zhu, J. Y.; Van Der Bruggen, B. Design and fabrication of microporous polyesteramide composite membranes for high-performance molecule/ion fractionation. *J. Membr. Sci.* **2026**, *737*, 124681.